ACS APPLIED MATERIALS & INTERFACES

Research Article

www.acsami.org

Hydrothermal Synthesis of Graphitic Carbon Nitride–Bi_2WO_6 Heterojunctions with Enhanced Visible Light Photocatalytic Activities

Yanlong Tian, Binbin Chang, Jiangli Lu, Jie Fu, Fengna Xi, and Xiaoping Dong*

Department of Chemistry, School of Sciences, Zhejiang Sci-Tech University, 928 Second Avenue, Xiasha Higher Education Zone, Hangzhou, China

Supporting Information

ABSTRACT: Graphitic carbon nitride (C_3N_4) was hybridized by Bi_2WO_6 via a hydrothermal method. The high-resolution transmission electron microscopy (HR-TEM) results reveal that an intimate interface between C_3N_4 and Bi_2WO_6 forms in the heterojunctions. The UV–vis diffuse reflection spectra show that the resulting C_3N_4–Bi_2WO_6 heterojunctions possess more intensive absorption within the visible light range in comparison with pure Bi_2WO_6. These excellent structural and spectral properties endowed the C_3N_4–Bi_2WO_6 heterojunctions with enhanced photocatalytic activities. Significantly, the optimum photocatalytic activity of the $0.5C_3N_4$–$0.5Bi_2WO_6$ heterojunction for the degradation of methyl orange (MO) was almost 3 and 155 times higher than those of either individual C_3N_4 or Bi_2WO_6. The possible photocatalytic mechanism with superoxide radical species as the main active species in photocatalysis is proposed on the basis of experimental results. Moreover, the heterojunction depicted high stability and durability during six successive cycles.

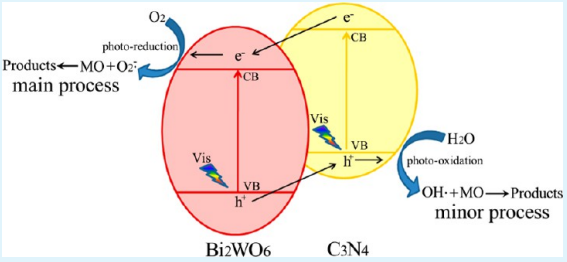

KEYWORDS: *C_3N_4, Bi_2WO_6, heterojunction, photocatalysis*

1. INTRODUCTION

As the environment deteriorates, green chemistry has become a necessary requirement for the sustainable development of human society. Among the various green chemical techniques, semiconductor photocatalysis has emerged as one of the most promising technologies because it represents an easy way to utilize the energy of either natural sunlight or artificial indoor illumination.[1−3] However, a large number of traditional photocatalysts (such as TiO_2, ZnO, SnO_2) are active only in the ultraviolet region due to their wide band gap and have moderate performance originating from the high recombination rate of photogenerated electron–hole pairs.[4−6]

Recently, the formation of heterojunction by coupling of two semiconductors with narrow band gap has attracted special attention as a novel strategy for overcoming two defects above of traditional photocatalysts.[7,8] Given that both of two semiconductors possess narrow band gap, such a heterogeneous system allows photocatalyst to utilize more visible light than traditional photocatalysts. What is more, the recombination of photogenerated electron–hole pairs can be effectively suppressed through a charge transfer between two semiconductors. Despite these advantages of heterojunction, it is not easy to construct such a system because the energy levels of coupling semiconductor must be well-matched overlapping band-structures. Therefore, the key link of constructing a heterojunction is to seek narrow band gap semiconductors with well-matched band-structure.

Very recently, Wang et al.[9] reported the development of a novel metal-free polymeric material, graphitic carbon nitride (C_3N_4), which exhibits high photocatalytic performance for hydrogen generation from water splitting and degradation of organic dyes under visible light irradiation. This organic semiconductor possesses a narrow band gap of 2.7 eV, which can make it utilize visible light directly without modification. In addition, unlike many photocatalysts of sulfide and oxynitride semiconductor, C_3N_4 is extremely stable with respect to thermal, chemical, and photochemical attack owing to its tri-s-triazine ring structure and high degree of condensation.[10] All these extraordinary properties of C_3N_4 imply that it should be an ideal photocatalytic material. To further improve the photocatalytic activity of C_3N_4, various strategies were adopted, including element doping,[11,12] introduction of mesoporous structure,[13,14] as well as coupling with heterogeneous semiconductors.[15−21] Up to now, several kinds of C_3N_4 based heterojunctions have been developed, for instance, C_3N_4–TaON,[15] C_3N_4–TiO_2,[16] C_3N_4–ZnO,[17] C_3N_4–$SrTiO_3$,[18] C_3N_4/$ZnWO_4$,[19] C_3N_4–BiOBr,[20] and C_3N_4–CdS,[21] etc.

Bismuth tungstate (Bi_2WO_6), as one of the simplest members of the Aurivillius oxide family, has a crystal structure composed of accumulated layers of alternating bismuth oxide $(Bi_2O_2)^{2+}$ layers and octahedral $(WO_4)^{2-}$ sheets.[22] The layered structure is favorable for charge transfer, and thus, Bi_2WO_6 exhibits excellent photocatalytic activity under visible light irradiation.[23−27] By comparing the energy levels of C_3N_4 with

Received: April 15, 2013
Accepted: July 10, 2013
Published: July 10, 2013

   dx.doi.org/10.1021/am4013819 | ACS Appl. Mater. Interfaces 2013, 5, 7079−7085

Bi_2WO_6, it is fortunate to find that the energy levels of C_3N_4 and Bi_2WO_6 are well-matched overlapping band-structures, suiting to construct a heterojunction with a high visible light catalytic activity. Most recently, Ge et al. have successfully prepared a C_3N_4–Bi_2WO_6 heterojunction by mixing and heating methods of C_3N_4 and Bi_2WO_4.[28] Nevertheless, the obtained insufficient contact interface by this simple mechanical mix would limit the transfer of photogenerated charges. Wang et al. have also synthesized the C_3N_4–Bi_2WO_6 heterojunction by chemisorbing C_3N_4 shells onto the surface of Bi_2WO_6 nanosheets.[29] Motivated by the above efforts, we herein presented a simple method to fabricate C_3N_4–Bi_2WO_6 heterojunction via a hydrothermal method. The visible light photocatalytic tests show that the present C_3N_4–Bi_2WO_6 heterojunction possesses excellent photocatalytic activity for degrading methyl orange (MO) under visible light irradiation, much higher than those of either individual C_3N_4 or Bi_2WO_6, as well as the nanosized TiO_2. Meanwhile, the resulting heterojunction also exhibits a high stability and durability after six successive cycles. The possible photodegradation mechanism of this heterojunction was also discussed based on experimental results.

2. EXPERIMENTAL SECTION

2.1. Synthesis. All reagents for synthesis and analysis were commercially available and used without further treatments. C_3N_4 was synthesized by thermal polycondensation of melamine, which was described in our previous report.[20,21] The resultant yellow product was collected and milled into a powder for further use.

C_3N_4–Bi_2WO_6 heterojunctions were obtained by a hydrothermal method with C_3N_4 and the precursor of Bi_2WO_6. In a typical procedure, a mixture of C_3N_4 and $Na_2WO_4{\cdot}2H_2O$ were added into 30 mL of deionized water, followed by vigorous stirring 3 h to obtain a uniform suspension. Meanwhile, a stoichiometric amount of $Bi(NO_3)_3{\cdot}5H_2O$ solid was dissolved in glacial acetic acid to obtain a clear solution. The solution was added rapidly to the suspension and subsequently stirred for another 3 h at room temperature. After carefully adjusting the pH value to ~8 using NaOH solution (1 M), the resulting mixture was transferred into a Teflon-lined steel autoclave, which was heated in an oven at 160 °C for 20 h. Subsequently, the precipitate was collected by filtration, washed with distilled water several times, and dried at 60 °C for 12 h. Finally, the obtained C_3N_4–Bi_2WO_6 heterojunctions were ground for further use. According to this method, different mass ratios of C_3N_4–Bi_2WO_6 at 7:3, 6:4, 5:5, 4:6, and 3:7 were prepared and denoted as $0.7C_3N_4$–$0.3Bi_2WO_6$, $0.6C_3N_4$–$0.4Bi_2WO_6$, $0.5C_3N_4$–$0.5Bi_2WO_6$, $0.4C_3N_4$–$0.6Bi_2WO_6$, and $0.3C_3N_4$–$0.7Bi_2WO_6$, respectively. The pure Bi_2WO_6 sample was synthesized under the same conditions in the absence of C_3N_4 powder.

As a reference, a mechanically mixed $0.5C_3N_4$–$0.5Bi_2WO_6$ sample was prepared by finely grinding 0.5 g of C_3N_4 with 0.5 g of Bi_2WO_6. Moreover, in order to compare photocatalytic activity with the present C_3N_4–Bi_2WO_6 heterojunction, other heterojunctions of $0.5C_3N_4$–$0.5Bi_2WO_6$–R (prepared according to ref 28), $0.5C_3N_4$–$0.5TiO_2$, and $0.5TiO_2$–$0.5Bi_2WO_6$, as well as a visible light responsive photocatalyst, N-modified TiO_2, were also prepared. Detailed procedures for the preparation of these four samples have been described in the Supporting Information.

2.2. Characterization. X-ray diffraction (XRD) patterns were monitored by a DX-2700 diffractometer (Dandong Haoyuan Instrument Co. Ltd., China) using Cu Kα radiation (λ = 0.15418 nm). Scanning electron microscopy (SEM) images and energy dispersive X-ray spectroscopy (EDS) maps were obtained with a Hitachi S-4800 Field emission scanning electron microscope. Transmission electron microscopy (TEM) observation and selected area electron diffraction (SAED) pattern were performed on a JEOL JEM-2100 electron microscope with an accelerating voltage of 200 kV. Fourier transform infrared (FT-IR) spectra were recorded on a Nicolet Avatar 370 spectrophotometer using the standard KBr disk method. Diffuse reflectance spectra were recorded on a Shimadzu 2450 UV–vis spectrometer with an integrating sphere using $BaSO_4$ as the reference.

2.3. Photocatalytic Tests. The photocatalytic activities of C_3N_4–Bi_2WO_6 heterojunction were evaluated by the degradation of MO and 2,4-dichlorophenol (2,4-DCP) in aqueous solution under visible light irradiation of a 300 W xenon lamp (HSX-F300, Beijing NBet) with the 400 nm cutoff filter. MO is a stable dye, and its photodegradation has been widely used as a representative reaction for examining the performance of many visible light active photocatalysts.[30,31] On the other hand, 2,4-DCP was selected since it has no absorption in the visible region. In each experiment, 100 mg of catalyst was suspended in an aqueous solution (100 mL) of MO or 2,4-DCP in a quartz glass reactor, which was cooled by recycled water to prevent the thermal catalytic effect. The initial concentrations of MO and 2,4-DCP solutions were 5 and 20 mg L^{-1}, respectively. Prior to irradiation, the suspension was stirred in the dark for 1 h to ensure the establishment of adsorption–desorption equilibrium. At given irradiation time intervals, 3 mL of the suspension was collected and subsequently centrifuged to remove the catalyst particles. The concentration was analyzed by measuring the maximum absorbance at 463 nm for MO and 283 nm for 2,4-DCP using a Shimadzu UV-2450 spectrophotometer.

3. RESULT AND DISCUSSION

3.1. Characterization of C_3N_4–Bi_2WO_6 Heterojunctions. XRD was used to characterize the crystal structure of the as-prepared C_3N_4–Bi_2WO_6 heterojunctions, as well as pure C_3N_4 and Bi_2WO_6 (Figure 1). Two distinct peaks of 13.04° and

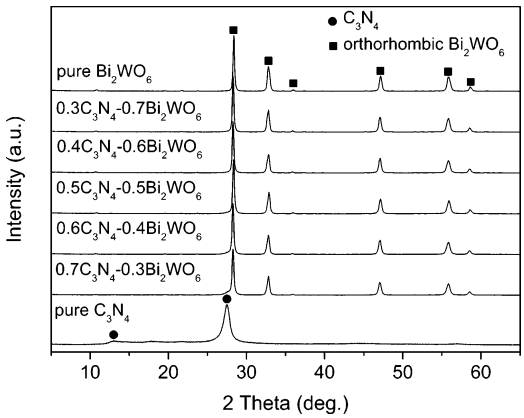

Figure 1. XRD patterns of C_3N_4, Bi_2WO_6, and C_3N_4–Bi_2WO_6 samples.

27.47° in the pure C_3N_4 sample can be indexed as the (100) and (002) diffractions for graphitic materials, respectively corresponding to the in-plane structural packing motif and interlayer stacking of aromatic segments.[11,32] The pure Bi_2WO_6 sample displays a series of narrow and sharp diffraction peaks, which can be identified as the orthorhombic phase of Bi_2WO_6 (JCPDS 73-1126). As coupling these two semiconductors, in C_3N_4–Bi_2WO_6 heterojunction samples similar diffractions to the pure Bi_2WO_6 are observed, indicating that the heterogeneous process would not bring any influence on the crystal structure. With respect to the invisibility of diffractions of C_3N_4 in heterojunctions, this is because the C_3N_4 layer was too thin.[19,29]

The morphology and microstructure of samples were investigated by SEM and TEM. A typically aggregated morphology with a large size and lamellar structure is found

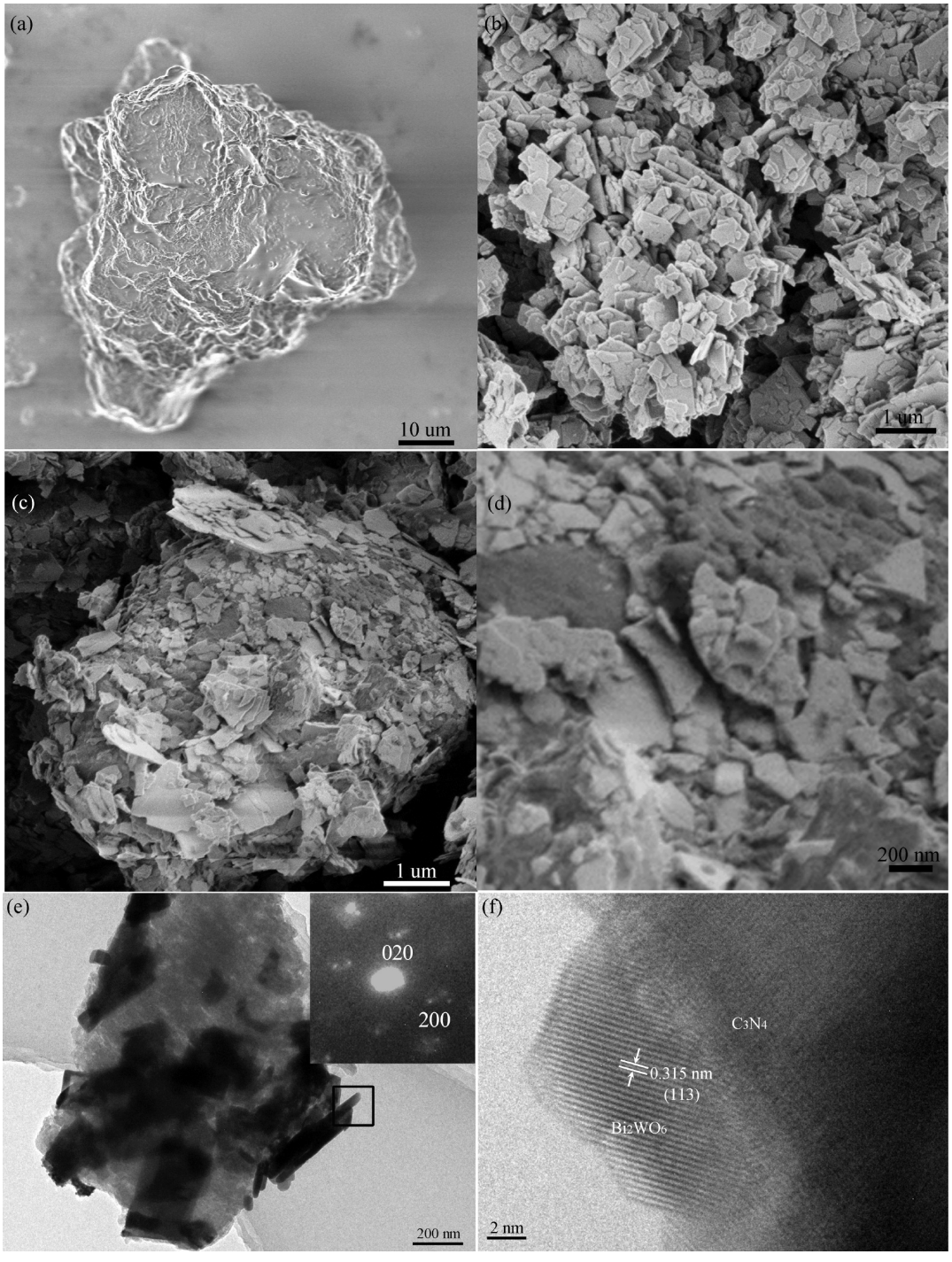

Figure 2. SEM images of (a) C_3N_4, (b) Bi_2WO_6, and (c) $0.5C_3N_4$–0.5 Bi_2WO_6 samples; (d) magnified SEM image, (e) TEM image and inserted SAED pattern of $0.5C_3N_4$–$0.5Bi_2WO_6$ sample; (f) HR-TEM image of $0.5C_3N_4$–$0.5Bi_2WO_6$ sample.

in the pure C_3N_4 sample (Figure 2a). The pure Bi_2WO_6 sample (Figure 2b) displays a number of flakelike morphologies with sizes of several hundred nanometers and thicknesses below 50 nm. After introducing Bi_2WO_6, amounts of nanoflakes are deposited on the surface of C_3N_4, resulting in the formation of a heterostructure (Figure 2c and d). The element mappings (Supporting Information Figure S1) of this heterostructure also imply the uniform distribution of Bi_2WO_6 on the surface of C_3N_4. The SEM images of C_3N_4–Bi_2WO_6 heterojunctions with various mass ratios are displayed in Supporting Information Figure S2. The size of Bi_2WO_6 in all these heterojunctions is similar to that of the pristine Bi_2WO_6. In addition, the density of Bi_2WO_6 nanoflakes deposited on the C_3N_4 surface increases step-by-step with the enhancement of Bi_2WO_6 content. In the case of $0.5C_3N_4$–$0.5Bi_2WO_6$ heterojunction, the surface of C_3N_4 has been covered by Bi_2WO_6 nanoflakes well. However, further increase of Bi_2WO_6 content results in a drastic overlapping of Bi_2WO_6 nanoflakes, which is helpless for fabrication of heterojunction with a close interface. Given to the observed morphology of Bi_2WO_6 in SEM images, the dark part with flake shape in the TEM image (Figure 2e) should be Bi_2WO_6 and the light part is C_3N_4, which further demonstrates

that Bi_2WO_6 nanoflakes have covered the surface of C_3N_4 well. An inserted SAED recorded on Bi_2WO_6 nanoflakes suggests a monocrystal structure. From the high-resolution TEM image of C_3N_4–Bi_2WO_6 heterojunction (Figure 2f), two phases of C_3N_4 and Bi_2WO_6 are clearly observed and closely contact to form an intimate interface. Because of the indistinct in-plane diffraction (100) in XRD pattern, the two-dimensional ordering of C_3N_4 is very weak and it is hard to find the lattice fringe of C_3N_4. Therefore, the clear lattice fringe in HR-TEM should be ascribed to Bi_2WO_6, and the calculated *d* value of 0.315 nm corresponds to the (113) crystallographic plane of the orthorhombic Bi_2WO_6 crystal, which is also in accordance with the XRD result in Figure 1. This tight coupling is favorable for the charge transfer between C_3N_4 and Bi_2WO_6 and promotes the separation of photogenerated electron–hole pairs, subsequently improving the photocatalytic activity. Moreover, this result also suggests that the C_3N_4–Bi_2WO_6 heterojunctions in structure are heterogeneous rather than a physical mixture of two separate phases of C_3N_4 and Bi_2WO_6.

The composition of C_3N_4–Bi_2WO_6 heterojunctions was further characterized by FT-IR spectroscopy (Figure 3). The

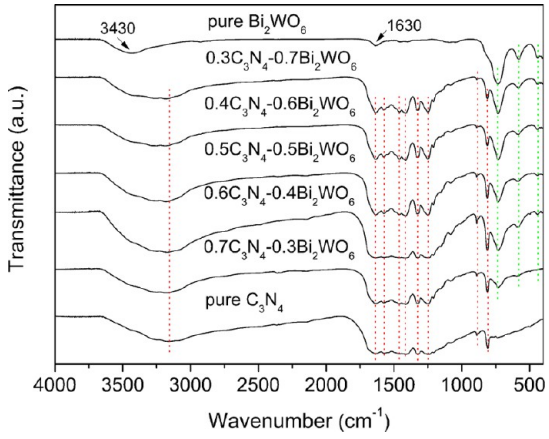

Figure 3. FT-IR spectra of C_3N_4, Bi_2WO_6, and C_3N_4–Bi_2WO_6 samples.

pure Bi_2WO_6 sample shows main absorption bands at 400–800 cm^{-1}, which are attributed to Bi–O, W–O stretching and W–O–W bridging stretching modes.[33] These peaks are still present in C_3N_4–Bi_2WO_6 heterojunctions, also suggesting that no structure change of Bi_2WO_6 appears during the hybridization process, which is consistent with the XRD result. The two prominent absorption bands at 3430 and 1630 cm^{-1} are assignable as the stretching and bending vibrations of the adsorbed water molecules.[34] In the case of pure C_3N_4, several typical absorption bands in the second region of 900–1800 cm^{-1} are attributed to either trigonal C–N(–C)–C (full condensation) or bridging C–NH–C units.[35] The former adsorption band is broad and centered at 3156 cm^{-1}, which can be ascribed to the stretching mode of N–H bond.[32,36] The band at 810 cm^{-1} originates from a breathing mode of s-triazine ring system.[32,37] Furthermore, all characteristic absorption bands of C_3N_4 and Bi_2WO_6 appear in the spectra of C_3N_4–Bi_2WO_6 heterojunctions, indicating the coexistence of these two semiconductors.

The optical property of C_3N_4–Bi_2WO_6 heterojunctions was examined using UV–vis diffuse reflectance spectroscopy. As shown in Figure 4, the pristine C_3N_4 holds an absorption edge

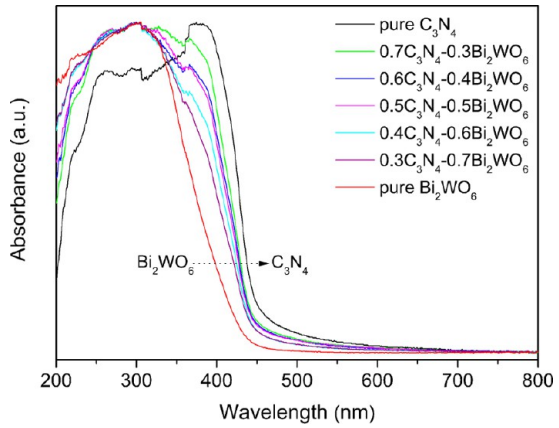

Figure 4. UV–vis diffuse reflectance spectra of C_3N_4, Bi_2WO_6, and C_3N_4–Bi_2WO_6 samples.

of ~460 nm, which can be assigned to a band gap of ~2.70 eV.[9] The absorption edge of pure Bi_2WO_6 sample was estimated at 441 nm corresponding to the band gap of 2.80 eV.[38] After combining the two semiconductors, C_3N_4–Bi_2WO_6 heterojunctions show more intensive absorption within the visible light range in comparison with pure Bi_2WO_6, and the visible light absorption intensity increases with increasing C_3N_4 content. In addition, this observation also clearly indicates that as-prepared C_3N_4–Bi_2WO_6 heterojunctions are able to work with visible light.

3.2. Photocatalytic Study of C_3N_4–Bi_2WO_6 Heterojunctions. On the basis of the above results, we have investigated the photodegradation of MO to evaluate the photocatalytic activity of as-synthesized C_3N_4–Bi_2WO_6 heterojunctions under visible light irradiation. As displayed in Figure 5a, the absorption of MO in the visible light region significantly deceases with the increase of irradiation time and nearly disappears after 2 h. In the meantime, no additional absorption appears in the ultraviolet region that indicates the complete destruction of aromatic structures. The characteristic absorption peak at 463 nm was employed to determine the degradation degree of MO, and the C/C_0 vs irradiation time was plotted in Figure 5b. MO molecules are very stable and experience almost no decomposition in the absence of catalyst, which excludes the possibility of photolysis in the present system. No obvious enhancement of degradation ratio was found when pure Bi_2WO_6 was used, which can be ascribed to its high recombination rate of photogenerated electron–hole pairs. As for the pure C_3N_4, it also shows poor activity, on which ~57% of MO is decomposed after irradiation for 120 min. After combining C_3N_4 and Bi_2WO_6, the photocatalytic activity of heterojunctions is significantly improved for the degradation of MO compared with the pure C_3N_4 and Bi_2WO_6. The photocatalytic activity first increases from $0.7C_3N_4$–$0.3Bi_2WO_6$ to $0.5C_3N_4$–$0.5Bi_2WO_6$ and, then, gradually decreases with the further increase of Bi_2WO_6 content. This result proves that too much Bi_2WO_6 in the heterojunction would create an unsuitable ratio between Bi_2WO_6 and C_3N_4, thus reducing photocatalytic activity of the heterojunction.[17] The highest activity is obtained over the $0.5C_3N_4$–$0.5Bi_2WO_6$ heterojunction, resulting in a 93% degradation ratio of MO within 120 min visible light irradiation. As a result, $0.5C_3N_4$–$0.5Bi_2WO_6$ heterojunction is selected for the following recycling experiments.

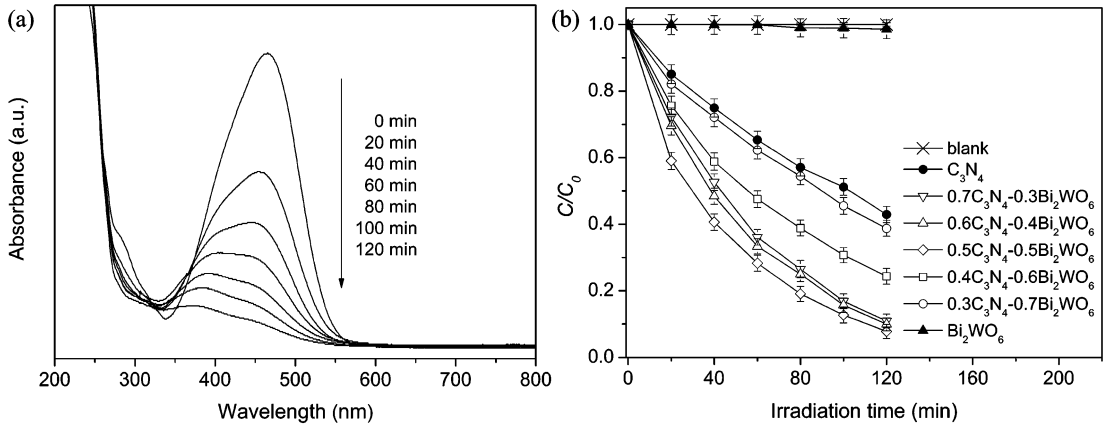

Figure 5. (a) Absorption spectra of MO with irradiation time over $0.5C_3N_4$–$0.5Bi_2WO_6$ heterojunction. (b) Degradation rates of MO under visible light irradiation without catalyst and in the presence of C_3N_4, Bi_2WO_6, and C_3N_4–Bi_2WO_6 samples.

To have a better understanding of the reaction kinetics of the MO degradation, the experimental data are fitted by a pseudo-first-order model. Supporting Information Figure S3a shows the first-order kinetics data for the photodegradation of MO using different catalysts. All fitting curves of the irradiation time (t) against $\ln(C_0/C)$ were nearly linear. As shown in Supporting Information Figure S3b, the rate constant (k) of C_3N_4–Bi_2WO_6 heterojunctions are obviously larger than those of individual C_3N_4 or Bi_2WO_6, respectively. This enhancement implies that the coexistence of C_3N_4 and Bi_2WO_6 gives rise to synergic effect for the C_3N_4–Bi_2WO_6 heterojunctions, which plays an important role in the separation of photogenerated electron–hole pairs.[28] To further confirm the heterojunction effect on the present C_3N_4–Bi_2WO_6 system, the photocatalytic experiment over the mechanically mixed $0.5C_3N_4$–$0.5Bi_2WO_6$ sample is also investigated and illustrated in Figure 6. The obtained

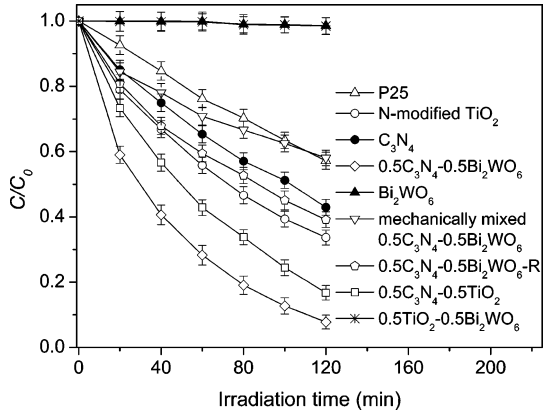

Figure 6. Degradation rates of MO under visible light irradiation in the presence of different catalysts.

activity of the mechanically mixed sample is much higher than that of pure Bi_2WO_6, a bit worse than that of pure C_3N_4, but much lower than that of the $0.5C_3N_4$–$0.5Bi_2WO_6$ heterojunction. The rate constant (k) of the $0.5C_3N_4$–$0.5Bi_2WO_6$ heterojunction is nearly 5 times larger than that of the mechanically mixed $0.5C_3N_4$–$0.5Bi_2WO_6$ sample (Supporting Information Figure S4b). This result demonstrates that coupling C_3N_4 with Bi_2WO_6 can form intimate interfaces between C_3N_4 and Bi_2WO_6 in C_3N_4–Bi_2WO_6 heterojunction, rather than form loose interfaces in the mechanically mixed sample.

For comparison, other heterojunctions of $0.5C_3N_4$–$0.5Bi_2WO_6$–R, $0.5C_3N_4$–$0.5TiO_2$ and $0.5TiO_2$–$0.5Bi_2WO_6$, as well as a visible light responsive photocatalyst of N-modified TiO_2 and a visible inactive photocatalyst of TiO_2 (Degussa P25) were also used for the degradation of MO (Figure 6). As expected, the visible inactive photocatalyst of P25 TiO_2 exhibits weak photocatalytic activity. The visible active $0.5C_3N_4$–$0.5TiO_2$ and N-modified TiO_2 samples, respectively, give the degradation ratio of 83% and 66% after 120 min of visible light irradiation, which are lower than that of the $0.5C_3N_4$–$0.5Bi_2WO_6$ heterojunction. However, another photocatalyst with visible light response, $0.5TiO_2$–$0.5Bi_2WO_6$, is almost inactive for the degradation of MO under visible light irradiation. This result indicates that heterojunction photocatalysts formed by combining two visible light driven semiconductors should be preferable to those coupled materials of a UV light active and a visible light responsive photocatalyst for the visible induced photocatalysis, in accordance with our previous report.[20,21] As for the sample of $0.5C_3N_4$–$0.5Bi_2WO_6$–R, which was prepared according to ref 28, the photocatalytic activity is also markedly improved compared with those of pure C_3N_4 and Bi_2WO_6, but lower than that of our $0.5C_3N_4$–$0.5Bi_2WO_6$ heterojunction. As displayed in Supporting Information Figure S4b, the rate constant (k) for MO photodegradation by our $0.5C_3N_4$–$0.5Bi_2WO_6$ heterojunction is 4.38, 2.29, 2.71, 1.42, and 147.63 times those of P25, N-modified TiO_2, $0.5C_3N_4$–$0.5Bi_2WO_6$–R, $0.5C_3N_4$–$0.5TiO_2$, and $0.5TiO_2$–$0.5Bi_2WO_6$, respectively, clearly demonstrating that the visible light photocatalytic activity of our $0.5C_3N_4$–$0.5Bi_2WO_6$ heterojunction is the highest among those of the investigated photocatalysts.

In view of the fact that MO is active to visible light, its photodegradation may be caused by a dye-sensitized path which does not require the band gap excitation of a nanocomposite catalyst.[39] To rule out this possibility and further identify the visible light activity of the $0.5C_3N_4$–$0.5Bi_2WO_6$ heterojunction, we also tested the degradation of 2,4-DCP that has no absorption in the visible light region (Supporting Information Figure S5a). Both pure C_3N_4 and Bi_2WO_6 samples show poor activities, on which only ~42% and 57% of 2,4-DCP are degraded after reacting 5 h, respectively. In contrast, 92% of 2,4-DCP molecules are decomposed under the same condition by $0.5C_3N_4$–$0.5Bi_2WO_6$ heterojunction, and its

dx.doi.org/10.1021/am4013819 | ACS Appl. Mater. Interfaces 2013, 5, 7079–7085

rate constant of ~0.5136 h^{-1} is nearly 4.63 and 3.08 times larger than those of individual C_3N_4 and Bi_2WO_6, respectively (Supporting Information Figure S5b). Moreover, its activity for the degradation of 2,4-DCP is also much better than that of a mechanically mixed one. The above results suggest that the contribution of dye-sensitization for the degradation of 2,4-DCP could be neglected compared to the photocatalytic degradation.

The stability and recyclability of photocatalysts are extremely important for practical applications. The cycling runs for the photodegradation of MO with $0.5C_3N_4$–$0.5Bi_2WO_6$ heterojunction were performed to evaluate its photocatalytic stability and recyclability. Figure 7 illustrates the relationship between

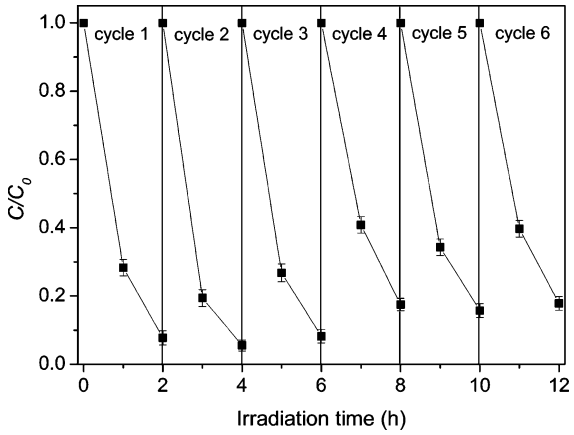

Figure 7. Cycling runs for the photocatalytic degradation of MO over $0.5C_3N_4$–$0.5Bi_2WO_6$ heterojunction under visible light irradiation.

degradation ratio of MO and cycle times. After reusing six cycles, the photodecomposition rate of MO still remains over 80%. In addition, XRD patterns of $0.5C_3N_4$–$0.5Bi_2WO_6$ heterojunction before and after reaction, as shown in Supporting Information Figure S6, distinctly reveal that the heterojunction is stable during the reaction.

3.3. Possible Photocatalytic Mechanism of C_3N_4–Bi_2WO_6 Heterojunctions. The above results reveal that the formation of heterojunction combining C_3N_4 with Bi_2WO_6 can enhance their photocatalytic activities under visible light irradiation. On the basis of experimental results, a possible visible light photocatalytic mechanism of the C_3N_4–Bi_2WO_6 heterojunction is proposed as illustrated in Figure 8. The conduction band (CB) and valence band (VB) potentials of C_3N_4 (−1.12 and 1.58 eV, respectively[9]) are more negative than those of Bi_2WO_6 (0.46 and 3.26 eV, respectively[38]), suggesting that C_3N_4 and Bi_2WO_6 match the band potentials in the C_3N_4–Bi_2WO_6 heterojunction.[26,40] Once the heterojunction is irradiated by visible light, both C_3N_4 and Bi_2WO_6 can be excited and produce photogenerated electron–hole pairs. Due to the well-matched overlapping band-structures and intimate interfaces (see Figure 2f), photogenerated electrons on the CB of C_3N_4 can easily transfer to the CB of Bi_2WO_6, and on the contrary, holes on the VB of Bi_2WO_6 spontaneously move to the VB of C_3N_4. This transference effectively suppresses the charge recombination, and thus results in an enhanced photocatalytic activity.

In order to further reveal the photocatalytic mechanism of C_3N_4–Bi_2WO_6 heterojunction, we also used the trapping experiments to determine the main active species in the photocatalytic process (Figure 9). The degradation efficiency of

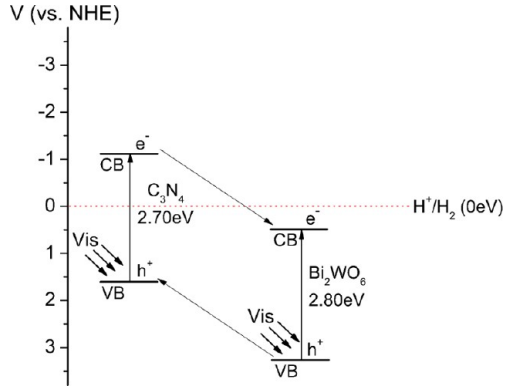

Figure 8. Schematic diagram of the separation and transfer of photogenerated charges in the C_3N_4–Bi_2WO_6 heterojunction under visible light irradiation.

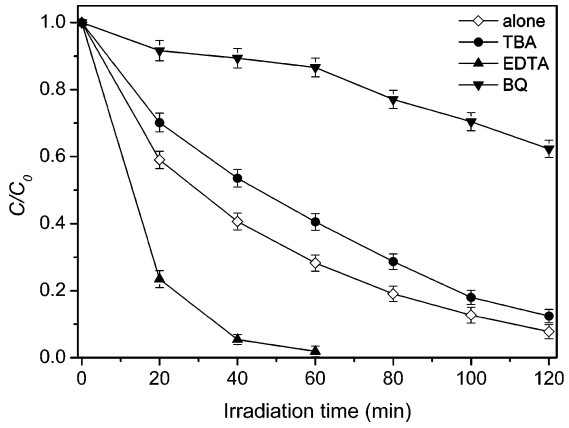

Figure 9. Photocatalytic degradation of MO over C_3N_4–Bi_2WO_6 heterojunction alone and with the addition of TBA, EDTA, or BQ.

MO is decreased slightly upon addition of tert-butyl alcohol (TBA, 2 mM, a hydroxyl radicals scavenger[41]), suggesting that hydroxyl radicals OH• are not the main active species for the degradation of MO. It is interesting to note that, when the scavenger disodium ethylenediaminetetraacetate (EDTA, 2 mM[42]) for photogenerated holes is added, the degradation behavior of MO is significantly improved. This result suggests that photogenerated holes are also not the main active species for the degradation of MO. As for the improved photocatalytic behavior, it should be attributed to EDTA as a scavenger that can effectively promote the photogenerated electron–hole pairs separation. However, once benzoquinone (BQ, 0.5 mM[43]), a scavenger for superoxide radicals $O_2^{\bullet-}$, is added to the reaction system, the degradation of MO is remarkably prohibited. This result demonstrates that $O_2^{\bullet-}$ should be the main active species in MO photodegradation.

4. CONCLUSIONS

In summary, we have successfully developed a C_3N_4–Bi_2WO_6 heterojunction via a hydrothermal method. The resulting C_3N_4–Bi_2WO_6 heterojunctions own a strong absorption in the visible light region and have obviously enhanced photocatalytic activities for the degradation of MO. The optimum photocatalytic activity of the $0.5C_3N_4$–$0.5Bi_2WO_6$ heterojunction for the degradation of (MO) was almost 3 and 155 times higher than those of individual C_3N_4 and Bi_2WO_6, respectively. This enhancement could be attributed to the high separation and

easy transfer of photogenerated electron−hole pairs at the intimate interface of heterojunctions, which can be reasonably ascribed to the well-aligned overlapping band-structures of C_3N_4 and Bi_2WO_6. Moreover, the heterojunction depicted an extreme stability that the photodecomposition rate of MO still remained over 80% after six cycles.

■ ASSOCIATED CONTENT

Supporting Information

Preparation details of $0.5C_3N_4$−$0.5Bi_2WO_6$−R, $0.5C_3N_4$−$0.5TiO_2$, $0.5TiO_2$−$0.5Bi_2WO_6$, and N-modified TiO_2. First-order kinetics data and value of the rate constant k for MO photodegradation over different photocatalysts (Figures S1 and S2). Degradation rates of 2,4-DCP under visible light irradiation in the presence of different catalysts and value of the rate constant k of the photodegradation of 2,4-DCP over different photocatalysts (Figure S3). XRD patterns of $0.5C_3N_4$−$0.5Bi_2WO_6$ heterojunction before and after the cycling photocatalytic experiments (Figure S4). This material is available free of charge via the Internet at http://pubs.acs.org.

■ AUTHOR INFORMATION

Corresponding Author

*E-mail: xpdong@zstu.edu.cn.

Notes

The authors declare no competing financial interest.

■ ACKNOWLEDGMENTS

We greatly acknowledge financial support from the National Natural Science Foundation of China (21001093), Qianjiang talent project of Zhejiang Province of China (2011R10048), and the Scientific Research Foundation for the Returned Overseas Chinese Scholars, State Education Ministry.

■ REFERENCES

(1) Tong, H.; Ouyang, S.; Bi, Y.; Umezawa, N.; Oshikiri, M.; Ye, J. *Adv. Mater.* **2012**, *24*, 229−251.
(2) Asahi, R.; Morikawa, T.; Ohwaki, T.; Aoki, K.; Taga, Y. *Science* **2001**, *293*, 269−272.
(3) Shi, R.; Lin, J.; Wang, Y.; Xu, J.; Zhu, Y. *J. Phys. Chem. C* **2010**, *114*, 6472−6477.
(4) Skinner, D. E.; Colombo, D. P.; Cavaleri, J. J.; Bowman, R. M. *J. Phys. Chem.* **1995**, *99*, 7853−7856.
(5) Ye, C.; Bando, Y.; Shen, G.; Golberg, D. *J. Phys. Chem. B* **2006**, *110*, 15146−15151.
(6) Chu, D.; Mo, J.; Peng, Q.; Zhang, Y.; Wei, Y.; Zhuang, Z.; Li, Y. *ChemCatChem* **2011**, *3*, 371−377.
(7) Cao, J.; Xu, B.; Luo, B.; Lin, H.; Chen, S. *Catal. Commun.* **2011**, *13*, 63−68.
(8) Zhang, L.; Wonga, K. H.; Chen, Z.; Yu, J. C.; Zhao, J.; Hu, C.; Chan, C. Y.; Wong, P. K. *Appl. Catal. A: Gen.* **2009**, *363*, 221−229.
(9) Wang, X.; Maeda, K.; Thomas, A.; Takanabe, K.; Xin, G.; Carlsson, J. M.; Domen, K.; Antonietti, M. *Nat. Mater.* **2009**, *8*, 76−80.
(10) Wang, Y.; Wang, X.; Antonietti, M. *Angew. Chem., Int. Ed.* **2012**, *51*, 68−89.
(11) Yan, S.; Li, Z.; Zou, Z. *Langmuir* **2010**, *26*, 3894−3901.
(12) Wang, X.; Chen, X.; Thomas, A.; Fu, X.; Antonietti, M. *Adv. Mater.* **2009**, *21*, 1609−1612.
(13) Zhang, Y.; Thomas, A.; Antonietti, M.; Wang, X. *J. Am. Chem. Soc.* **2009**, *131*, 50−51.
(14) Yan, H. *Chem. Commun.* **2012**, *48*, 3430−3432.
(15) Yan, S.; Lv, S.; Li, Z.; Zou, Z. *Dalton Trans.* **2010**, *39*, 1488−1491.
(16) Yan, H.; Yang, H. *J. Alloys Compd.* **2011**, *509*, L26−L29.
(17) Sun, J.; Yuan, Y.; Qiu, L.; Jiang, X.; Xie, A.; Shen, Y.; Zhu, J. *Dalton Trans.* **2012**, *41*, 6756−6763.
(18) Xu, X.; Liu, G.; Randorn, C.; Irvine, J. T. S. *Int. J. Hydrogen Energy* **2011**, *36*, 13501−13507.
(19) Wang, Y.; Wang, Z.; Muhammad, S.; He, J. *CrystEngComm* **2012**, *14*, 5065−5070.
(20) Fu, J.; Tian, Y.; Chang, B.; Xi, F.; Dong, X. *J. Mater. Chem.* **2012**, *22*, 21159−21166.
(21) Fu, J.; Chang, B.; Tian, Y.; Xi, F.; Dong, X. *J. Mater. Chem. A* **2013**, *1*, 3083−3090.
(22) Xu, C.; Wei, X.; Guo, Y.; Wu, H.; Ren, Z.; Xu, G.; Shen, G.; Han, G. *Mater. Res. Bull.* **2009**, *44*, 1635−1641.
(23) Zhang, L.; Zhu, Y. *Catal. Sci. Technol.* **2012**, *2*, 694−706.
(24) Cheng, H.; Huang, B.; Dai, Y.; Qin, X.; Zhang, X.; Wang, Z.; Jiang, M. *J. Solid State Chem.* **2009**, *182*, 2274−2278.
(25) Tang, J.; Zou, Z.; Ye. *J. Catal. Lett.* **2004**, *92*, 53−56.
(26) Ge, M.; Li, Y.; Liu, L.; Zhou, Z.; Chen, W. *J. Phys. Chem. C* **2011**, *115*, 5220−5225.
(27) Zhang, H.; Liu, L.; Zhou, Z. *Phys. Chem. Chem. Phys.* **2012**, *14*, 1286−1292.
(28) Ge, L.; Han, C.; Liu, J. *Appl. Catal. B: Environ.* **2011**, *108−109*, 100−107.
(29) Wang, Y.; Bai, X.; Pan, C.; He, J.; Zhu, Y. *J. Mater. Chem.* **2012**, *22*, 11568−11573.
(30) Yang, G.; Jiang, Z.; Shi, H.; Xiao, T.; Yan, Z. *J. Mater. Chem.* **2010**, *20*, 5301−5309.
(31) Lin, X.; Huang, T.; Huang, F.; Wang, W.; Shi, J. *J. Phys. Chem. B* **2006**, *110*, 24629−24634.
(32) Yan, S.; Li, Z.; Zou, Z. *Langmuir* **2009**, *25*, 10397−10401.
(33) Yu, J.; Xiong, J.; Cheng, B.; Yu, Y.; Wang, J. *J. Solid State Chem.* **2005**, *178*, 1968−1972.
(34) Chen, Z.; Lin, B.; Xu, B.; Li, X.; Wang, Q.; Zhang, K.; Zhu, M. *J. Porous Mater.* **2011**, *18*, 185−193.
(35) Niu, P.; Zhang, L.; Liu, G.; Cheng, H. *Adv. Funct. Mater.* **2012**, *22*, 4763−4770.
(36) Bojdys, M. J.; Müller, J. O.; Antonietti, M.; Thomas, A. *Chem.—Eur. J.* **2008**, *14*, 8177−8182.
(37) Dong, F.; Wu, L.; Sun, Y.; Fu, M.; Wu, Z.; Lee, S. C. *J. Mater. Chem.* **2011**, *21*, 15171−15174.
(38) Zhang, Z.; Wang, W.; Wang, L.; Sun, S. *ACS Appl. Mater. Interfaces* **2012**, *4*, 593−597.
(39) He, J.; Benko, G.; Korodi, F.; Polivka, T.; Lomoth, R.; Akermark, B.; Sun, L.; Hagfeldt, A.; Sundstrom, V. *J. Am. Chem. Soc.* **2002**, *124*, 4922−4932.
(40) Zhang, H.; Wu, D.; Tang, Q.; Liu, L.; Zhou, Z. *J. Mater. Chem. A* **2013**, *1*, 2231−2237.
(41) Minero, C.; Mariella, G.; Maurino, V.; Vione, D.; Pelizzetti, E. *Langmuir* **2000**, *16*, 8964−8972.
(42) Elovitz, M. S.; Gunten, U. V. *Ozone Sci. Eng* **1999**, *21*, 239−260.
(43) Zhang, Y.; Zhang, N.; Tang, Z.; Xu, Y. *Chem. Sci.* **2013**, *4*, 1820−1824.